Wall-Normal Focused Laser Differential Interferometry

Jens Lunte* and Erich Schülein†
DLR, German Aerospace Center, 37073 Göttingen, Germany

https://doi.org/10.2514/1.J063258

A new approach for measuring boundary-layer disturbances with focused laser differential interferometry (FLDI) for planar models is presented. By integrating a glass window into a flat plate, the optical axis was aligned normal to the model surface, and the focal plane was set inside the boundary layer. By determining the extent of the sensitive volume along the optical axis and calculating the analytical transfer function of the setup, the implications of the FLDI properties on the measured data are analyzed. Measurements performed on a flat plate at Mach 6 are used to demonstrate the effects of the laminar–turbulent transition on the spectral distribution of the power density and to explicitly verify the detectability of the expected second-mode instabilities. Advantages and disadvantages of the proposed setup compared to the conventional one are discussed.

I. Introduction

A PRUDENT design of a hypersonic flight vehicle in terms of its drag and thermal protection necessitates a reliable prediction of the transition location on the vehicle. Despite the endeavors of the last decades, the obtained insights into the laminar–turbulent transition phenomena are still insufficient for providing the required prediction capability, so fundamental experimental studies on hypersonic transition stay relevant. However, the reliable time-resolved measurement of flow parameters in the transitional hypersonic boundary layer is an exceptionally challenging task. Because of the high mean flow velocity and broad range of scales involved—from the largest eddy scales where most of the energy is present to the smallest ones where kinetic energy dissipates into heat—the frequency spectrum is particularly broadband and high-frequency. In addition, the transition process is very susceptible to external influences and can readily be affected by the insertion of a measuring probe. The focused laser differential interferometry (FLDI), introduced by Smeets and George [1] to measure the freestream density disturbances in supersonic wind tunnels, satisfies the requirements of a nonintrusive and broadband measurement technique. Although the FLDI method had been known since 1973 at the latest, a real breakthrough was only achieved when Parziale [2] successfully demonstrated its application in the investigation of boundary-layer instabilities on a cone.

The central element of the FLDI technique consists of two parallel, slightly shifted light cones, which are focused at the measuring plane, and later interfere due to density differences at both focal positions. Outside the focal plane, the diameter of both light beams increases, and the beams partly overlap. Besides the overlap, the instrument's sensitivity to density disturbances outside the focal plane decreases rapidly due to the spatial averaging [3]. To measure the density disturbances of the boundary layer, the optical axis is usually aligned spanwise through the boundary layer of the model. But this approach has several problems. First, several coherent structures or turbulent spots arranged side by side within the boundary layer can simultaneously pass through the sensitive volume of the FLDI setup. Second, the assumptions for deriving analytical transfer functions of the FLDI technique [3–6] are rarely satisfied in real flow situations and therefore cannot be used for data correction. Third, flat plate models pose a particular challenge, because the light cones outside the focal plane are shadowed by the model itself (Fig. 1, red beam path). To overcome the third problem, Houpt and Leonov [7,8] modified the standard FLDI setup by using cylindrical lenses to focus the light in a plane parallel to the flat plate (Fig. 1, blue beam path). Although turbulence spectra could be measured, the unwanted sensitivity outside the focal plane increased compared to the conventional setup.

In the present work a new FLDI approach [9] for investigating the boundary layer on a flat plate is presented, which was also applied by Maszkiewicz et al. [10]. By integrating a glass window into a flat plate (Fig. 1, green beam path) and aligning the optical axis normal to the surface, the standard FLDI setup with the superior spatial filtering can be used. The proposed setup differs from the variant with the surface mirror known from Smeets and George [1] in that both separate beams pass the object of interest only once. The intrinsic measurement properties of the top-viewing FLDI, resulting from a vertical integration of the probe volume, are analyzed here and compared with those of a conventional FLDI. In particular, the ability of the top-viewing FLDI to detect the second Mack modes as well as turbulent patches in a transitional boundary layer on a flat plate is verified here.

II. Experimental Program

A. FLDI Characteristics via Laboratory Pretests

The intrinsic properties of the proposed FLDI system were first investigated analytically, and then the frequency response was documented by a preliminary test with a free jet. The studied FLDI setup (Fig. 2) used a $\lambda_{\mathrm{OBIS}} = 660$ nm laser beam (*OBIS 660LX*), which was focused by a microscopic lens on a pinhole (PH) with a diameter of 50 μm to obtain a well-defined focus. After the pinhole, an iris (I) reduced the beam diameter to the free aperture of the following 1″ Wollaston prism (WP). A linear polarization filter (LPF) set the polarization of the laser beam to 45° relative to the optical axis of the following WP. The WP split the beam in two orthogonal partial beams with a separation angle of $\varphi_{\mathrm{WP}} = 2'$ in streamwise direction. A 2″ lens (L), placed one focal length ($f_L = 300$ mm) behind the WP, fixed the distance between both beam axis to $\Delta x = 175$ μm and focused the beam profiles. After the focal plane, the partial beams expanded again, were focused by a second lens, and were recombined by a second WP. By displacing the second WP across the optical axis [11], the FLDI setup was adjusted to maximal sensitivity. After passing another LPF, the partial beams interfered with each other. The interference intensity due to the optical path difference Δs_{opt} was converted to a voltage signal by a photo diode (PD, Thorlabs DETA36A2) and recorded by a Tektronix DPO 7254 oscilloscope at a sampling frequency of 25 MHz.

To quantify the response of the FLDI to disturbances outside the focal plane, test measurements with a free jet were performed as usual (Fig. 3). The jet was generated via a nozzle with an opening

Presented as Paper 2023-3449 at the AIAA Aviation 2023 Forum, San Diego, CA, June 12–16, 2023; received 29 June 2023; revision received 13 November 2023; accepted for publication 14 November 2023; published online Open Access 20 December 2023.

*Research Scientist, Department of High Speed Configurations, Institute of Aerodynamics and Flow Technology; jens.lunte@dlr.de.

†Senior Research Scientist, Department of High Speed Configurations, Institute of Aerodynamics and Flow Technology; erich.schuelein@dlr.de.

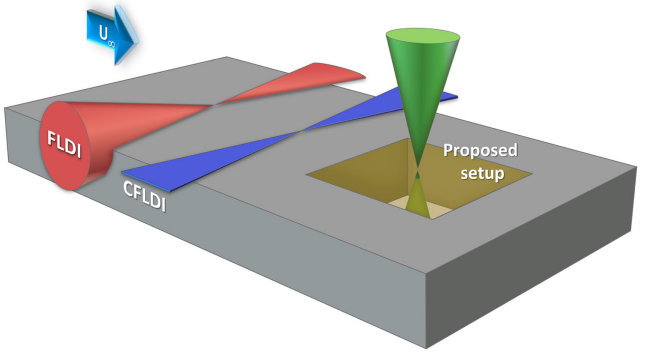

Fig. 1 Sketch of FLDI beam paths at 2D models to illustrate the beam blockage with standard FLDI and two solutions. Sketch based on Ref. [8].

diameter of 0.6 mm, which was placed approximately 10 diameters ($\Delta y_{\text{jet}} \approx 6$ mm) below the optical axis. At the applied pressure of 1.85 bar, the exit velocity of the free jet is just below the speed of sound. As depicted in Fig. 3, by traversing the nozzle along the optical axis (Δz_{jet}), the spatial filtering outside the focal plane can be studied.

B. Freestream Disturbances in the RWG

The flow measurements were conducted at the Mach 6 conditions of the DLR Ludwieg-Tube Facility in Göttingen (RWG) [12,13] (Fig. 4). For the freestream measurements the laser beam was conventionally guided through both windows of the wind tunnel, and the focal plane was set at the symmetry axis of the circular Laval nozzle. The test section diameter is 0.5 m, so the enlarged beam diameter attenuates the density fluctuations of the wind tunnel boundary layer, especially at higher frequencies. The freestream disturbances were measured at 9 discrete freestream unit Reynolds numbers $Re_{1,\infty}$ between $Re_{1,\infty} = 4 \cdot 10^6$ m^{-1} and $Re_{1,\infty} = 24 \cdot 10^6$ m^{-1}.

C. Boundary-Layer Instabilities on a Flat Plate

The instabilities in the transitional boundary layer were investigated by FLDI on a flat-plate model mounted in the RWG. The flat-plate model is 400 mm wide, is 669 mm long, and has a leading-edge radius of 0.1 mm. The leading edge of the flat plate in the symmetry plane shifted to the level of its surface is the origin of the used coordinate system (cf. Fig. 5). A 150-mm-wide cutout between $x = 96$ mm and $x = 496$ mm enables the flush installation of an insert adapted to the respective measurement technique. In the current study an insert with an embedded glass window was mounted into the flat plate. Additionally, a 46×270 mm^2 duct was installed between the wind tunnel wall and the bottom of the glass insert. The upstream face of the duct was covered with a wedge shaped wind deflector to ease the start of the wind tunnel flow. The duct completely prevents the interaction of the laser beams with the flow below the base plate. Therefore, a phase shift between the partial beams can only result from effects on the upper side of the flat plate. The flow density fluctuations above the flat plate were measured at 11 streamwise positions from 171 to 421 mm in 25 mm steps at four $Re_{1,\infty}$ (cf. Table 1).

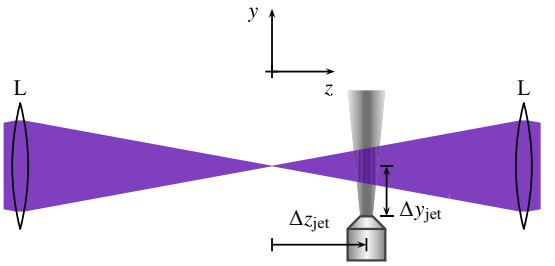

Fig. 3 Zoomed-in sketch of the FLDI setup from a different viewing angle with the jet to investigate the FLDI response.

III. Results and Discussion

A. FLDI Characteristics

Experimentally, FLDI detects a voltage signal from the photodiode, whose value is determined by the phase difference between beam pair to interference. The voltage U of the photo diode can be converted to the optical path difference Δs_{opt} using [14]

$$\Delta s_{\text{opt}} = \frac{\lambda_{\text{OBIS}}}{2\pi} \arcsin\left(\frac{U}{U_0} - 1\right) \tag{1}$$

Here U_0 denotes the measured voltage at $\Delta s_{\text{opt}} = 0$, which is typically taken immediately before the wind tunnel start. Alternatively, U_0 can be approximated by the average of the measured signal. The latter method was used in this study to account for a potential change in the transmitted light intensity due to a possible soiling of the windows when starting the wind tunnel run. Additionally, Δs_{opt} was high pass filtered at $f = 500$ Hz to reduce the effects of mechanical vibrations caused by the wind tunnel operation on the measurement signal.

From the theoretical side, Δs_{opt} can be calculated using the Gladstone–Dale relation [15] ($n = \rho K_{\text{GD}} + 1$) by the integral over the density difference along the optical axis (z-axis) with [2,4]

$$\Delta s_{\text{opt}} = K_{\text{GD}} \int \Delta\rho(z) \mathrm{d}z \tag{2}$$

Here $\Delta\rho(z)$ is an effective density difference, averaged over the beam profile intensity, and K_{GD} is the Gladstone–Dale constant. The integral and the effective density difference make it impossible to invert Eq. (2) for a direct calculation of the density field from the measured optical path difference. However, the amplitude response of the FLDI system can be studied by analyzing generic density fields [3–6]. The amplitude response is mainly a result of two effects: the fixed beam distance Δx and the averaging over the beam diameter along the optical axis. The impact of the former effect was estimated by simplifying the FLDI as two perfect point measurements separated by Δx. The transfer function $H_{\Delta x}$ of a generic 1D density disturbance along the x-direction with the frequency f and the phase velocity u_{ph} is [3,4]

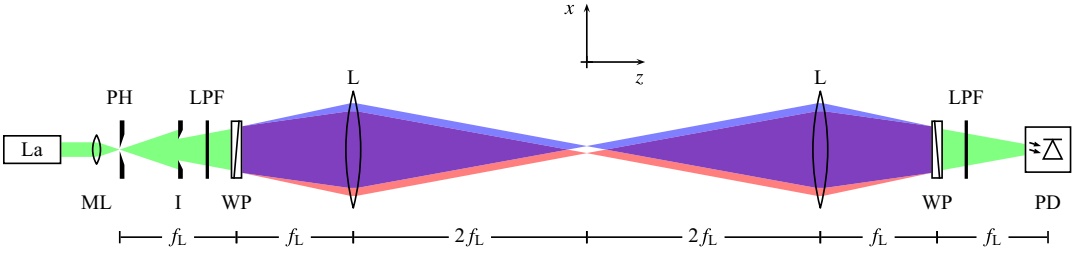

Fig. 2 Sketch of the FLDI setup. The separated beams are depicted in blue and red. Overlapping regions are violet.

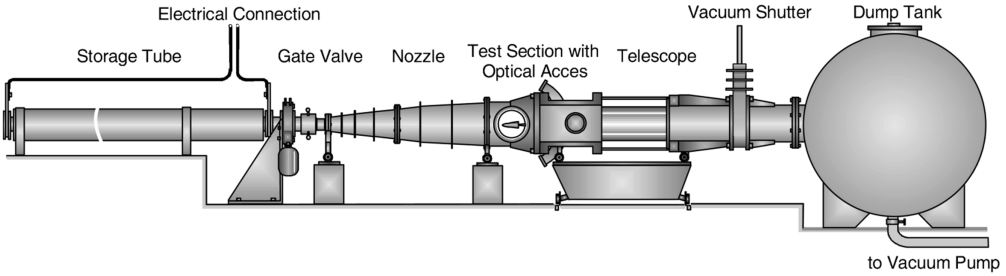

Fig. 4 Sketch of the Ludwieg-Tube Facility at DLR Göttingen [12].

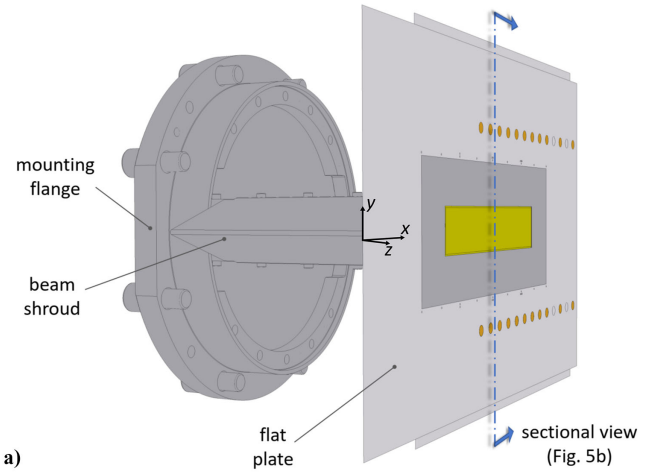

Fig. 5 Sketch of the flat plate model with the duct (a) and a sectional view with the FLDI beam path (b).

Table 1 Representative flow parameters at the investigated unit Reynolds numbers at the RWG

$Re_{1,\infty}$, m^{-1}	p_0, MPa	T_0, K	p_∞, Pa	T_∞, K	ρ_∞, kg/m^3	u_∞, m/s
$8 \cdot 10^6$	1.08	543	700	66.6	0.037	978
$14 \cdot 10^6$	1.89	543	1220	66.6	0.064	978
$19 \cdot 10^6$	2.55	543	1650	66.6	0.086	978
$24 \cdot 10^6$	3.32	543	2090	66.6	0.109	978

$$H_{\Delta x}(f) = \frac{u_{\mathrm{ph}}}{\pi f \Delta x} |\sin(\pi f \Delta x / u_{\mathrm{ph}})| \tag{3}$$

Figure 6 shows the transfer function predicted by Eq. (3) for the current test conditions assuming $u_{\mathrm{ph}} = 0.9 u_\infty$ in accordance with Ref. [16]. It indicates a decreasing amplitude response for $f >$ 1 MHz and no response in direct vicinity of $f \approx 5$ MHz, which means that the chosen distance between the two focal points attenuates the measurable amplitude for high frequencies and must be considered during the interpretation of the data. To what extent this theoretical results can be observed in the experimental data depends whether the stated assumptions are valid for the current setup, which will be addressed in Sec. III.C.

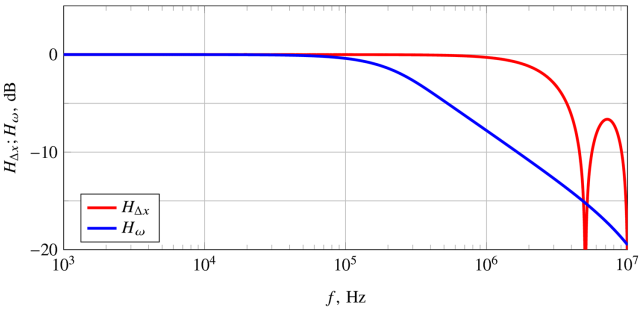

Fig. 6 Analytical transfer functions $H_{\Delta x}$ and H_ω due to the finite distance of the two FLDI beams and the spatial filtering outside the focal plane, respectively.

Outside the focal plane, the beam diameter increases, the beams overlap, and the density fluctuation field is spatially averaged over the beam profiles and integrated along the beam path. The attenuation of the measurement signal due to this spatial averaging effect was analyzed in previous works [3,4]. One analytical transfer function H_ω for a symmetrical 2D density field around the focal plane was presented by Schmidt and Shepherd [3] and is given by

$$H_\omega(k) = \frac{\pi \omega_0 \sqrt{2\pi}}{k L \lambda_{\mathrm{OBIS}}} \exp\left(-\frac{\omega_0^2 k^2}{8}\right) \mathrm{erf}\left(\frac{k L \lambda_{\mathrm{OBIS}}}{2\sqrt{2}\pi\omega_0}\right) \tag{4}$$

The predicted attenuation of H_ω is visualized in Fig. 6 for a minimal Gaussian beam waist radius $\omega_0 = 25$ μm, our wind tunnel half width $L = 250$ mm, and the wave numbers calculated by $k = 2\pi f / u_{\mathrm{ph}}$. The plot of H_ω illustrates that when investigating the freestream disturbances in the RWG over the entire width of the wind tunnel, a reduction of the measurable amplitudes has to be anticipated at higher frequencies due to the spatial filtering of the FLDI system. For the investigation of boundary-layer instabilities at the flat plate, the spatial filtering effect should be of negligible importance, as the disturbances are localized within the boundary layer and thus close to the focal plane.

Besides theoretical analysis, the response of the FLDI system was also documented experimentally with a jet, which was traversed along the optical axis (see Fig. 3). The attenuation of the density fluctuation amplitude outside the focal plane can be observed by means of the power spectral density (PSD) in Fig. 7. The further the jet moves away from the focal plane, the lower the PSD and thus the response of the FLDI technique. Furthermore, Fig. 7 shows that the attenuation outside the focal plane is frequency dependent. The higher the frequency, the stronger the attenuation outside the focal plane. The $-5/3$ roll-off of the incompressible Kolmogorov scaling is plotted in Fig. 7 in comparison to the obtained PSDs. Comparing it with only the dark blue line ($\Delta z_{\mathrm{jet}} = 0$ mm), one sees that the measured paths over large frequency ranges follow relatively well the trend for incompressible fully turbulent flows. A clear limit to

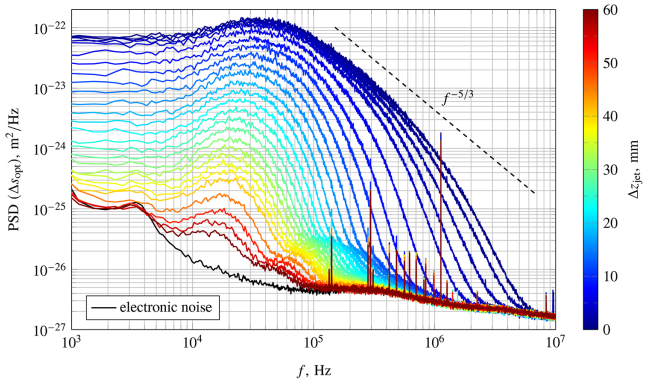

Fig. 7 PSD of the free jet measurement for various positions along the optical axis.

the region, e.g., with a steeper slope, indicating insufficient local resolution in the experiment, cannot be determined from these data. The maximum PSD value found for $\Delta z_{jet} = 0$ mm is about at 40 kHz, corresponding to most-energy-containing eddy scales of about 7 mm (assuming a convection velocity of 280 m/s). The shift of the peak to smaller frequencies observed with increasing Δz_{jet} is a direct consequence of the decrease in local resolution (averaging over an increasing cross-sectional area of the light cone) and was clearly predicted in simulations by Fulghum (see Fig. 3.26 from Ref. [4]).

To evaluate the length of the sensitive volume along the optical axis, the RMS value of each measurement position is shown in Fig. 8. The RMS value dropped to $1/e$ of the maximum value at roughly 12 mm outside the focal plane, and above 35 mm the density disturbances of the free jet are indistinguishable from the background noise. The extent of the sensitive area along the optical axis implies that the measurable boundary-layer disturbances on the flat plate will be superimposed with the disturbances of the freestream, because the boundary-layer thickness is expected to be in the single-digit millimeter range (see Table 2).

B. Freestream Disturbances in the RWG

The analysis of sensitive volume along the optical axis of the used FLDI system revealed that the boundary-layer instabilities cannot be measured independently from the freestream disturbances. To identify the effects of boundary-layer transition in the presence of the freestream disturbances, the density fluctuations in the empty measurement section of the RWG were measured first. The PSDs of the freestream disturbances in Fig. 9a obviously show a sufficiently high signal-to-noise ratio, which steadily increases with increasing

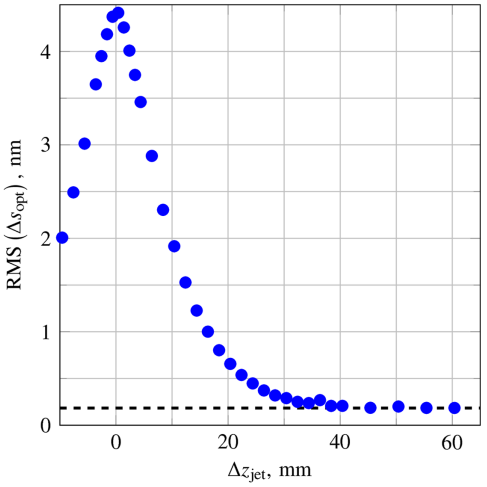

Fig. 8 RMS value of the free jet measurement for various positions along the optical axis.

Table 2 Experimentally determined averaged f_{Mack} with their standard deviation and the other CFD-based values used for the scaling of the second Mack mode

$Re_{1,\infty}$, m^{-1}	x, mm	f_{Mack}, kHz	δ_{99}, mm	δ_{infl}, mm	$\delta_{99}/\delta_{infl}$, -	u_∞, m/s
$24 \cdot 10^6$	221	187(15)	2.75	1.64	1.68	978
$24 \cdot 10^6$	246	192(16)	2.82	1.73	1.63	978
$24 \cdot 10^6$	271	172(14)	2.88	1.82	1.58	978
$24 \cdot 10^6$	296	168(14)	2.94	1.89	1.55	978
$19 \cdot 10^6$	271	177(14)	3.03	2.02	1.50	978
$19 \cdot 10^6$	296	146(12)	3.10	2.10	1.48	978
$19 \cdot 10^6$	321	144(12)	3.16	2.18	1.45	978
$14 \cdot 10^6$	321	140(11)	3.42	2.51	1.36	978
$14 \cdot 10^6$	346	123(10)	3.49	2.60	1.34	978
$14 \cdot 10^6$	371	114(9)	3.55	2.68	1.33	978
$8 \cdot 10^6$	371	94(8)	4.20	3.41	1.23	978
$8 \cdot 10^6$	396	85(7)	4.29	3.53	1.21	978
$8 \cdot 10^6$	421	96(8)	4.38	3.64	1.21	978

Reynolds number in the flow. Since the $Re_{1,\infty}$ increase was realized here only by increasing the flow density, the scaling of Δs_{opt} with ρ_∞ in Fig. 9b unifies the distribution of the freestream PSD over the entire Reynolds number range.

The plotted straight line with a slope of −3.5, which appears to describe the current data quite well in the frequency range above ≈50 kHz, is consistent not only with the roll-off of the Pitot-pressure spectra from numerous previous studies in conventional hypersonic wind tunnels (see review in Ref. [17]), but also with the roll-off found in previously published FLDI freestream spectra in comparable low-enthalpy hypersonic tunnels [16,18].

The reason for the peculiarity of the PSD distribution in the frequency domain, which is noticeable as a slight kink (or even an S-beat at higher $Re_{1,\infty}$) just above 100 kHz in current data sets as well as in freestream spectra of Weisberger et al. [16], remains unexplained for the time being and will be addressed in more detail in the future. For $f < 3$ kHz, mechanical vibrations during the operation of the wind tunnel dominate the signal. Above this, the density disturbances of the freestream are visible and form a maximum between $f \approx 10$ and 20 kHz. For $f > 30$ kHz, the PSD decreases steadily to the noise level. It is commonly agreed that the main source for free flow disturbances in conventional supersonic and hypersonic wind tunnels is the radiation of acoustic waves from the turbulent boundary layer at the wind tunnel walls into the measurement section [19–21]. Accordingly, the measured shape of the PSD spectrum (Fig. 9b) is consistent with the FLDI results from other wind tunnels [16,18]. A comparison regarding the amplitude of the freestream disturbances is void, since the absolute value of the optical phase difference (Δs) depends on the individual measurement setup, and thus the prerequisite for an objective evaluation is missing. Although the laser beams are expanded as they traverse the nozzle boundary layer and thus primarily high-frequency signals are attenuated, studies [4,18,22] showed that the measurement signal may also contain shares of the low frequency density fluctuations from the nozzle boundary layer.

C. Boundary-Layer Instabilities on a Flat Plate

Knowing the spectral distribution of the freestream fluctuations, the boundary-layer instabilities on the flat plate can be studied. The superposition of both types of density fluctuations can be observed in the PSD of Fig. 10. For measurement positions near the leading edge, where the boundary layer is laminar, the measured PSD resembles the spectrum of the freestream. Only when the intensity of the density fluctuations inside the boundary layer increases due to the transition process and exceeds the level of the measurement noise and freestream disturbances, a change in PSD can be observed. At the latest for $x > 346$ mm at $Re_{1,\infty} = 14 \cdot 10^6$ m^{-1}

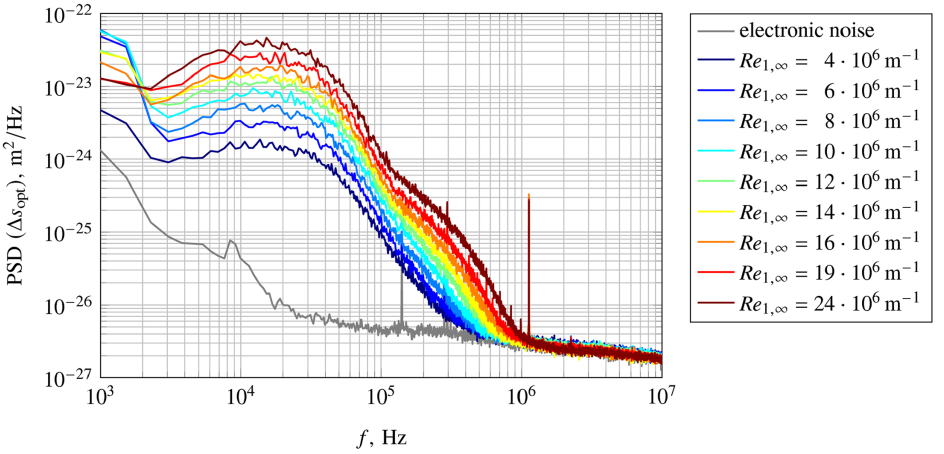

a) The amplitude of the free flow disturbances increases with $Re_{1,\infty}$ or, more precisely, with ρ_∞

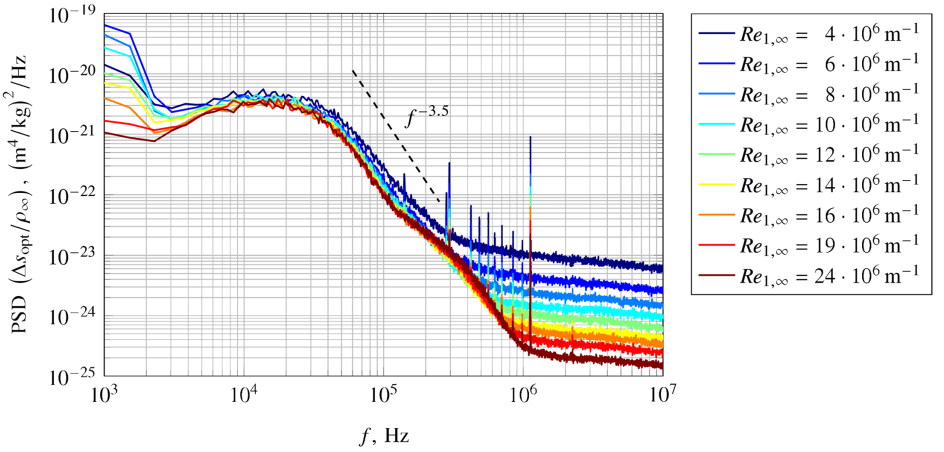

b) Scaling the measurement signal with ρ_∞ yields a nearly uniform spectrum

Fig. 9 PSD of the freestream disturbances for the RWG Mach 6 nozzle.

(Fig. 10a), the growth of the perturbations due to the laminar–turbulent transition at the flat plate becomes visible and leads to a broader frequency spectrum. A plausible path of the frequency spectrum in the direction of a turbulent flow up to the last investigated position $x = 421$ mm can be seen.

Figure 10b shows the development of PSD along the streamwise direction for $Re_{1,\infty} = 24 \cdot 10^6$ m^{-1}. Due to the higher $Re_{1,\infty}$, the transition begins at a smaller x coordinate and completes over a shorter distance. The PSD deviates from the freestream disturbance spectrum at $x = 271$ mm and becomes more broadband up to $x = 396$ mm. The PSD at $x = 421$ mm shows no significant changes from the directly upstream position, indicating a completed transition already at the $x = 396$ mm location.

Although the turbulent boundary layer has a broadband spectrum, the PSD drastically decreases for $f > 2$ MHz. It is remarkable that all PSD distributions reach the level of noise in a common way and are constricted exactly at the frequency of 5 MHz, which was predicted to be a blind spot due to the chosen distance between the focal points of the FLDI setup (cf. Fig. 6). The FLDI measurements of Weisberger et al. [16] in the boundary layer of a cone model conducted with a spanwise-oriented beam path show a similar but less salient local minimum in the PSD. The authors of Refs. [3,4] argued in the context of spanwise-oriented FLDI setups, that this insensitive frequency is a consequence of the idealized approach and should not be present in real measurements, which explains the attenuated impact of the insensitive frequency in the experiments of Weisberger et al. [16]. For wall-normal-oriented FLDI setups, the assumption of a 1D disturbance for Eq. (3) seems to be quite justified, because the strongest density fluctuations are expected to be located near the boundary-layer edge at approximately $0.75\delta - 0.9\delta$ [23,24], and the focal plane of the FLDI was placed inside the boundary layer with the focal points aligned in flow direction. The stricter abidance of the theoretical approach leads to a more salient effect of the predicted insensitive frequency compared to the conventional FLDI beam orientation, which could be utilized in subsequent theoretical or experimental studies. For example, the insensitive frequency correlates with the phase velocity ($f_{crit} = u_{ph}/\Delta x$) according to Eq. (3). Therefore, an experimental determination of the insensitive frequency may provide an indirect method for obtaining the averaged phase velocity of turbulent spots by means of single point FLDI.

The PSDs in Fig. 10b display a complex superposition of disturbances attributable to the free incoming flow, the turbulent boundary layer at the nozzle wall, and the transitional boundary layer at the flat plate in combination with the attenuation of the fluctuation amplitude predicted by the transfer functions. Due to the complex measurement situation, there is no reliable basis for the interpretation of the visible slopes.

Although the depiction of the second Mack modes as local peaks in the power density spectrum was accomplished in other publications with conventional FLDI setups [16,25], these peaks are absent in Figs. 10a and 10b. The absence of the second mode peaks is probably related to the spatial arrangement of the beam path. Due to the wall-normal beam orientation, the freestream disturbances occupy the major part of the sensitive volume of the FLDI setup and overlay the weaker second Mack modes. Additionally, the number of detectable density fluctuations in the boundary layer is reduced, because the intersection between the measurement volume and the boundary layer is significantly smaller than in the case of a conventional spanwise alignment of the optical axis.

To investigate whether second Mack modes are detectable at all with the current FLDI setup, the measurement signal at $x = 396$ mm for $Re_{1,\infty} = 14 \cdot 10^6$ m^{-1} was analyzed using a wavelet transformation (Fig. 11). Figure 11a shows the measurement signal

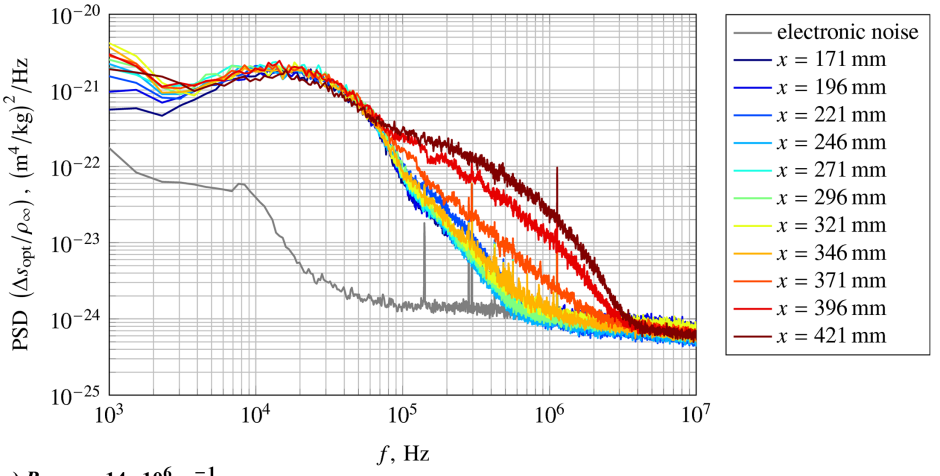

a) $Re_{1,\infty} = 14 \cdot 10^6\ m^{-1}$

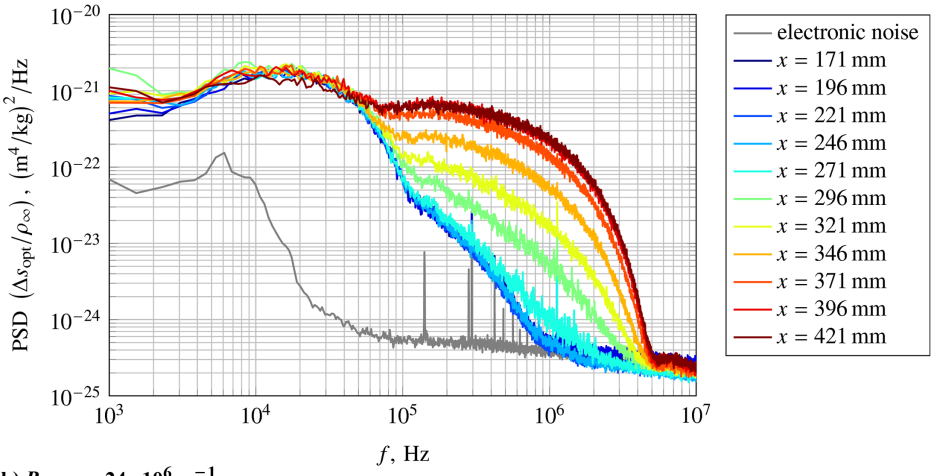

b) $Re_{1,\infty} = 24 \cdot 10^6\ m^{-1}$

Fig. 10 PSD of the transitional boundary layer at various streamwise positions for two $Re_{1,\infty}$. The laminar–turbulent transition leads to broadband frequency spectra.

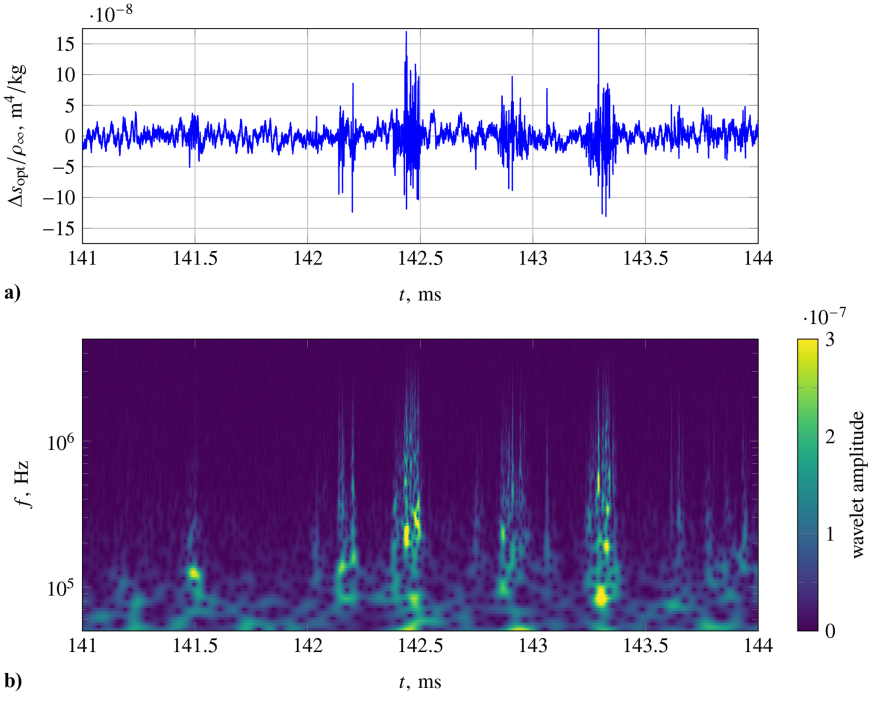

Fig. 11 Time trace (a) of the FLDI measurement at $x = 396$ mm for $Re_{1,\infty} = 14 \cdot 10^6\ m^{-1}$ and the corresponding wavelet transformation (b).

detected in the transitional boundary layer over the time. The recorded signal contains characteristic sections in which the wavelet transform shows a particularly broadband frequency spectrum (Fig. 11b). These fluctuations are caused by turbulent spots traversing the sensitive volume of the FLDI setup (e.g., $t = 142.5$ ms and $t = 143.3$ ms). Besides the turbulent spots, a probable passage of a second mode packet can be observed at $t = 141.5$ ms, which was identified by its narrowband frequency peak at $f = 125$kHz. A bandpass-filtered signal of this density disturbance is shown in Fig. 12 and looks like a wave packet, which is typical for a second Mack mode instability [16].

To convincingly verify that second Mack modes can be detected at the RWG with the current FLDI setup, the main frequency of the narrowband density disturbances is determined from the wavelet transformation and checked with an established scaling law. Since no reliable algorithm for the detection of the potential second Mack modes could be found, the determination was done by hand. The experimentally determined frequencies f_{Mack} were scaled according to the established correlation $(u_\infty/(f_{\mathrm{Mack}}\delta_{99}) = 2)$ of Demetriades [26] and Stetson et al. [27]. For the scaling, the value of u_∞ was taken from Table 1, and the boundary-layer thickness δ_{99} was determined via 2D laminar CFD simulations with isothermal walls ($T_w = 293.15$ K) for the specific flow conditions using the DLR-TAU-Code [28]. Figure 13a shows the averaged result of the scaled frequencies for the individual measurement positions, plotted over the Reynolds number Re_x based on the streamwise flat plate coordinate x. The used values are listed in Table 2. The error bars illustrate the scatter of the measurement data via the 1σ environment. The deviation of the

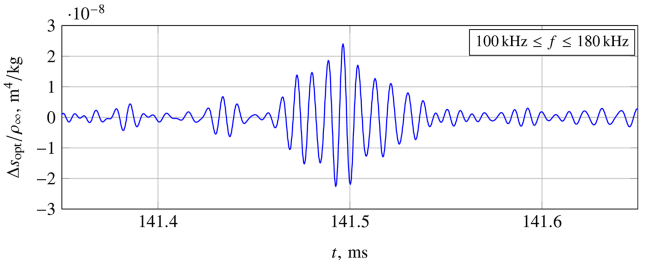

Fig. 12 The bandpass-filtered measurement section of the disturbance at $t = 141.5$ ms in Fig. 11 resembles a wave packet.

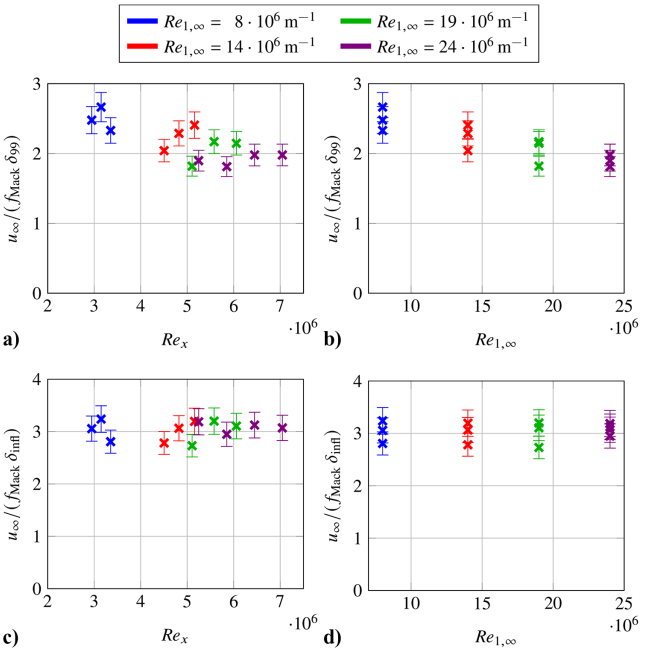

Fig. 13 Examination of an established scaling law for the frequency of the second Mack modes (a, b) and an improved modification (c, d).

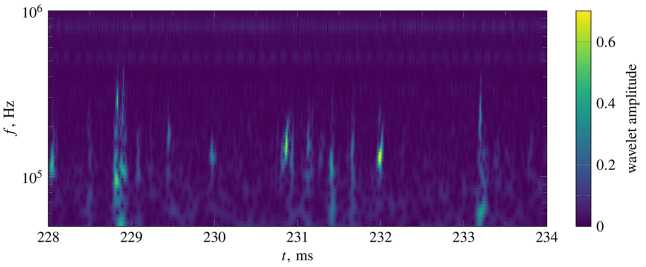

Fig. 14 Wavelet transformation of a PCB measurement at $x = 397.33$ mm for $Re_{1,\infty} = 14 \cdot 10^6$ m^{-1}.

experimental results from the expected value 2 is within the correlation accuracy [26,27], where the values for comparable temperature ratios T_w/T_0 are between 2 and 2.5. The data points in Fig. 13a show a convergence to the value $u_\infty/(f_{\mathrm{Mack}}\delta_{99}) = 2$ with increasing Re_x, which is not observable in Demetriades [26] or Stetson et al. [27]. Figure 13b illustrates that the found tendency is related to an $Re_{1,\infty}$ effect, which is not satisfactorily accounted for in the scaling and shall be improved with the following attempt.

Kuehl [29] analyzed the second Mack modes by linear stability analysis and showed that the calculated eigenmodes are confined within the boundary layer by a local impedance minimum. The upper limit of the impedance minimum correlated with the inflection point of the acoustic field impedance Z_F of the base flow. The acoustic field impedance describes the resistance of a medium to the propagation of an acoustic wave and is given by $Z_F = \rho c$ [30], where ρ and c are the local density and the speed of sound. By determining the wall-normal distance δ_{infl} to the inflection point of the acoustic field impedance via the conducted TAU simulations and replacing δ_{99} in the scaling of f_{Mack} with δ_{infl}, no $Re_{1,\infty}$ effect is visible in Figs. 13c and 13d. Column $\delta_{99}/\delta_{\mathrm{infl}}$ in Table 2 shows that by changing the parameter describing the boundary-layer height dimension, the Re_x dependency of the scaled frequencies is affected. The length δ_{infl} might be more closely correlated to the trapping mechanism of the second Mack modes than δ_{99} and therefore yield the improved constancy of the scaled frequencies in Fig. 13c compared to Fig. 13a.

In addition to the investigation of the transitional boundary layer with FLDI, measurements of the boundary-layer pressure fluctuations with PCB sensors were also conducted on the flat plate model for the same flow conditions [9]. Figure 14 shows the wavelet transformation of the PCB measurement signal and complements the inspection of the boundary-layer fluctuations at the measuring position of Fig. 11 with a second independent measurement technique. Since Fig. 14 also exhibits narrowband fluctuations with a frequency around 125 kHz (e.g., $t = 230$ ms and $t = 232$ ms), the PCB data support the hypothesis that second Mack modes were detected by the wall-normal FLDI setup. A detailed discussion of the PCB data is beyond the scope of the current paper and is postponed to a future publication.

IV. Conclusions

To investigate boundary-layer instabilities on planar models using the advantageous measurement characteristics of the standard FLDI setup, a glass window was built into a flat plate and the beam was directed normal to the wall. The proposed concept was verified and discussed by the investigation of characteristic flow structures inside a transitional hypersonic boundary layer. The boundary-layer disturbances at various streamwise positions were measured, and the corresponding PSD distributions became more broadband as the laminar–turbulent transition progressed. The measured PSD bandwidth of the turbulent boundary layer was shown to be limited by the amplitude response of the FLDI technique, which is constrained by the chosen distance between the two focal points, whereby the critical frequency could be accurately predicted with the theory. The determination of the sensitivity of the FLDI setup to disturbances outside the focal plane indicated a significant superposition of the boundary-layer

instabilities and the freestream disturbances; therefore, no second Mack modes are directly visible in the PSD spectra. However, the investigation of time traces demonstrated the intermittent character of the transitional boundary layer and allowed the identification of turbulent spots and narrowband fluctuations, which were identified as second Mack modes. Supplementary PCB data at the same measurement position show identical narrowband fluctuations and provide further affirmation that the wave packets in the FLDI data represent second Mack modes. The frequency of the presumed second modes was verified by an established scaling law, but the scaled frequencies indicated a remaining unit Reynolds number effect. By exchanging the boundary-layer height in the scaling law with the height of the impedance inflection point inside the boundary layer, the remaining $Re_{1,\infty}$ effect could be compensated. The observed improvement can be attributed to the closer relation between the impedance profile and the trapping mechanism of acoustic modes.

Testing the reorientation of the beam path when using the FLDI technique on plate models revealed some advantages and disadvantages compared to the conventional experimental setup. For example, it could be demonstrated that the orientation of the optical axis normal to the model surface affects the detectability of density fluctuations within the boundary layer. This effect occurs due to the unfavorably short integration length within the boundary layer relative to that in the outer flow. The extensive overlap of the frequency ranges of the external flow and the flat-plate boundary layer complicated the detection of the second Mack modes in the current work. An additional study of the eigenmodes for a wall-normal and spanwise beam orientation of the FLDI could yield theoretical insights as to whether the sensitivity is affected by the beam orientation. Although the detection of weak density fluctuations is hampered, the wall-normal beam orientation also offers exclusive advantages. On the one hand, the ambiguity of multiple simultaneous wave packets within the sensitive volume is avoided. On the other hand, the theoretical assumptions for the derivation of analytic transfer functions seem to be fulfilled, which enables the potential correction of the measurement signal. As the projection of the volume sensitive within the boundary layer onto the surface of the flat plate practically yields a point, the wall-normal beam orientation enables the investigation of spanwise varying flows, which extends the area of applications for FLDI.

References

[1] Smeets, G., and George, A., "Laser-Differential Interferometer Applications in Gas Dynamics," Tech. Rept., Inst. Saint-Louis Rept. 28/73, Translated 1996 by A. Goetz, Nov. 1973.

[2] Parziale, N., "Slender-Body Hypervelocity Boundary-Layer Instability," Ph.D. Dissertation, California Inst. of Technology, Pasadena, CA, 2013.

[3] Schmidt, B. E., and Shepherd, J. E., "Analysis of Focused Laser Differential Interferometry," *Applied Optics*, Vol. 54, No. 28, 2015 pp. 8459–8472.
https://doi.org/10.1364/AO.54.008459

[4] Fulghum, M. R., "Turbulence Measurements in High-Speed Wind Tunnels Using Focusing Laser Differential Interferometry," Ph.D. Dissertation, Pennsylvania State Univ., Pennsylvania, 2014.

[5] Settles, G. S., and Fulghum, M. R., "The Focusing Laser Differential Interferometer, an Instrument for Localized Turbulence Measurements in Refractive Flows," *Journal of Fluids Engineering*, Vol. 138, No. 10, 2016, Paper 101402.
https://doi.org/10.1115/1.4033960

[6] Hameed, A., and Parziale, N. J., "Focused Laser Differential Interferometric Investigation of Turbulent Jet Spectra," *Journal of Spacecraft and Rockets*, Vol. 59, No. 5, 2022, pp. 1565–1573.
https://doi.org/10.2514/1.A35292

[7] Houpt, A. W., and Leonov, S. B., "Focused Laser Differential Interferometer for Supersonic Boundary Layer Measurements on Flat Plate Geometries," *2018 Plasmadynamics and Lasers Conference*, AIAA Paper 2018-3434, 2018.
https://doi.org/10.2514/6.2018-3434

[8] Houpt, A., and Leonov, S., "Cylindrical Focused Laser Differential Interferometer," *AIAA Journal*, Vol. 59, No. 4, 2021, pp. 1142–1150.
https://doi.org/10.2514/1.J059750

[9] Lunte, J., "Shock-Induced Flow Separation in Transitional Boundary Layers," Ph.D. Dissertation (in German), Georg-August-Universität Göttingen, Göttingen, 2021.
https://doi.org/10.53846/goediss-9050

[10] Maszkiewicz, S. A., Gillespie, G., and Laurence, S. J., "Experimental Investigation of Transitional, Sharp-Fin-Induced Shock-Wave/Boundary-Layer Interactions at Mach 6," *AIAA Scitech 2022 Forum*, AIAA Paper 2022-1818, 2021.
https://doi.org/10.2514/6.2022-1818

[11] Ramprakash, A., McIntyre, T., Wheatley, V., and Mee, D., "Performance Analysis of FLDI Technique Using Turbulent Jets," *IX Australian Conference on Laser Diagnostics*, The Univ. of Adelaide, Adelaide, Australia, 2019, p. 4.

[12] Schülein, E., "Skin Friction and Heat Flux Measurements in Shock/Boundary Layer Interaction Flows," *AIAA Journal*, Vol. 44, No. 8, 2006, pp. 1732–1741.
https://doi.org/10.2514/1.15110

[13] Wagner, A., Schülein, E., Petervari, R., Hannemann, K., Ali, S. R. C., Cerminara, A., and Sandham, N. D., "Combined Free-Stream Disturbance Measurements and Receptivity Studies in Hypersonic Wind Tunnels by Means of a Slender Wedge Probe and Direct Numerical Simulation," *Journal of Fluid Mechanics*, Vol. 842, May 2018, pp. 495–531.
https://doi.org/10.1017/jfm.2018.132

[14] Parziale, N. J., Shepherd, J. E., and Hornung, H. G., "Reflected Shock Tunnel Noise Measurement by Focused Differential Interferometry," *42nd AIAA Fluid Dynamics Conference and Exhibit*, AIAA Paper 2012-3261, 2012.
https://doi.org/10.2514/6.2012-3261

[15] Gladstone, J. H., and Dale, T. P., "XIV. Researches on the Refraction, Dispersion, and Sensitiveness of Liquids," *Philosophical Transactions of the Royal Soc. of London*, Vol. 153, Dec. 1863, pp. 317–343.
https://doi.org/10.1098/rstl.1863.0014

[16] Weisberger, J. M., Bathel, B. F., Herring, G. C., King, R. A., Chou, A., and Jones, S. B., "Two-Point Focused Laser Differential Interferometry Second-Mode Measurements at Mach 6," *AIAA Aviation 2019 Forum*, AIAA Paper 2019-2903, 2019.
https://doi.org/10.2514/6.2019-2903

[17] Duan, L., Choudhari, M. M., Chou, A., Munoz, F., Radespiel, R., Schilden, T., Schröder, W., Marineau, E. C., Casper, K. M., Chaudhry, R. S., Candler, G. V., Gray, K. A., and Schneider, S. P., "Characterization of Freestream Disturbances in Conventional Hypersonic Wind Tunnels," *Journal of Spacecraft and Rockets*, Vol. 56, No. 2, 2019, pp. 357–368.
https://doi.org/10.2514/1.A34290

[18] Gillespie, G. I., Ceruzzi, A. P., and Laurence, S. J., "A Multi-Point Focused Laser Differential Interferometer for Characterizing Freestream Disturbances in Hypersonic wind Tunnels," *Experiments in Fluids*, Vol. 63, No. 11, 2022, p. 180.
https://doi.org/10.1007/s00348-022-03522-6

[19] Pate, S. R., and Schueler, C. J., "Radiated Aerodynamic Noise Effects on Boundary-Layer Transition in Supersonic and Hypersonic Wind Tunnels," *AIAA Journal*, Vol. 7, No. 3, 1969, pp. 450–457.
https://doi.org/10.2514/3.5128

[20] Schopper, M. R., "Interaction of Aerodynamic Noise with Laminar Boundary Layers in Supersonic Wind Tunnels," NASA CR-3621, 1984.

[21] Schneider, S. P., "Developing Mechanism-Based Methods for Estimating Hypersonic Boundary-Layer Transition in Flight: The Role of Quiet Tunnels," *Progress in Aerospace Sciences*, Vol. 72, Jan. 2015, pp. 17–29.
https://doi.org/10.1016/j.paerosci.2014.09.008

[22] Benitez, E. K., Borg, M. P., Hill, J. L., Aultman, M. T., Duan, L., Running, C. L., and Jewell, J. S., "Quantitative Focused Laser Differential Interferometry with Hypersonic Turbulent Boundary Layers," *Applied Optics*, Vol. 61, No. 31, 2022, pp. 9203–9216.
https://doi.org/10.1364/AO.465714

[23] Stetson, K., and Kimmel, R., "On Hypersonic Boundary-Layer Stability," *30th Aerospace Sciences Meeting and Exhibit*, AIAA Paper 1992-0737, 1992.
https://doi.org/10.2514/6.1992-737

[24] Benitez, E. K., Jewell, J. S., and Schneider, S. P., "Focused Laser Differential Interferometry with Contoured Tunnel Windows," *AIAA Journal*, Vol. 59, No. 2, 2021, pp. 419–429.
https://doi.org/10.2514/1.J060081

[25] Parziale, N., Shepherd, J., and Hornung, H., "Differential Interferometric Measurement of Instability at Two Points in a Hypervelocity Boundary Layer," *51st AIAA Aerospace Sciences Meeting Including the New Horizons Forum and Aerospace Exposition*, AIAA Paper 2013-0521, 2013, pp. 750–754.
https://doi.org/10.2514/1.J052013

[26] Demetriades, A., "Laminar Boundary Layer Stability Measurements at Mach 7 Including Wall Temperature Effects," Tech. Rept. AFOSR TR-77-1311, Ford Aerospace and Communications Corp., 1977.

[27] Stetson, K. F., Thompson, E. R., Donaldson, J. C., and Siler, L. G., "Laminar Boundary Layer Stability Experiments on a Cone at Mach 8, Part 5—Tests with a Cooled Model," *20th Fluid Dynamics, Plasma Dynamics and Lasers Conference*, AIAA Paper 1989-1895, 1989. https://doi.org/10.2514/6.1989-1895

[28] Schwamborn, D., Gerhold, T., and Heinrich, R., "The DLR TAU-Code: Recent Applications in Research and Industry," *European Conference on Computational Fluid Dynamics*, ECCOMAS CFD, TU Delft, Delft, The Netherlands, 2006, p. 25. https://doi.org/10.2514/1.J061234

[29] Kuehl, J. J., "Thermoacoustic Interpretation of Second-Mode Instability," *AIAA Journal*, Vol. 56, No. 9, 2018, pp. 3585–3592. https://doi.org/10.2514/1.J057015

[30] Meyer, E., and Neumann, E.-G., *Physikalische und Technische Akustik*, 2nd ed., Vieweg+Teubner Verlag, Wiesbaden, 1974, Chap. 1. https://doi.org/10.1007/978-3-322-91086-8

L. Ukeiley
Associate Editor